Is it possible for Fe^{2+} to approach protoporphyrin IX from the side of Tyr-13 in *Bacillus subtilis* ferrochelatase? An answer from QM/MM study

Yaxue Wang · Yong Shen

Abstract We previously reported the insertion process of the ferrous ion into the protoporphyrin IX from the side of the residue His-183 (*J. Inorg. Biochem.* 103 (2009) 1680–1686). Sellers et al. suggested that the ferrous ion probably approaches the protoporphyrin IX via the opposite side in the human enzyme. In this paper, we simulated the insertion process of Fe^{2+} into the protoporphyrin IX from the side of the residue Tyr-13 at the opposite site of His-183 by QM/MM method on *Bacillus subtilis* ferrochelatase. The model was built with Fe^{2+} ion coordinated by Tyr-13, His-88 and two water molecules. Geometries were optimized at the BP86/6-31G* level and energies were calculated at the B3LYP/6-311+G(2d,2p) level. The overall process involves the displacement of the residues Tyr-13, His-88 and one water molecule and deprotonation of the porphyrin ring. All the local minimum structures and energy barriers were obtained and an optimal insertion pathway was suggested. The rate-determining step is the removing of the second proton from the porphyrin accompanied by the formation of the fourth Fe-N bond with an energy barrier of 138.00 kJ/mol.

Keywords Ferrochelatase · Metallation · Protoporphyrin IX · QM/MM

Y. Wang · Y. Shen (✉)
School of Chemistry and Chemical Engineering,
Sun Yat-sen University,
510275, Guangzhou, People's Republic of China
e-mail: cessy@mail.sysu.edu.cn

Y. Wang
School of College of Food Science and Engineering,
Northwest A & F University,
712100, Yangling, People's Republic of China

Introduction

Ferrochelatase is the terminal enzyme in heme biosynthesis and catalyzes the insertion of ferrous iron into protoporphyrin IX to form protoheme IX (heme) [1]. Heme, as a cofactor of various proteins and enzymes, perform vital functions in the human body such as cellular respiration and the transport of electrons and oxygen. Mutations in the ferrochelatase gene can lead to the disease erythropoietic porphyria (EPP) [2]. Overproduction of protoporphyrin and its deposition in skin result in the light-sensitive dermatitis [3]. In some cases this may even lead to fatal liver damage [4].

The mechanism of protoporphyrin metallation catalyzed by ferrochelatase has attracted much interest[5–13]. Hansson et al. [12] suggested that the insertion of the metal ion into the protoporphyrin IX occurs by binding with His-183 and Glu-264 for *Bacillus subtilis* ferrochelatase. The human and yeast enzymes also support that the residue His-183 is involved in the ferrous ion binding and inserting into the protoporphyrin IX [10, 13]. In our previous report [14], we studied the process of Fe^{2+} entering into the portoporphyrin IX from the side of the residue His-183 in *Bacillus subtilis* ferrochelatase. The rate-determining step is the formation of the first Fe-N bond. However, the position of the catalytic metal binding site and the path of the metal into the porphyrin in ferrochelatase are still a matter of debate. Sellers et al. [15] suggested that the ferrous ion probably approaches the protoporphyrin IX via the opposite side (the side of Met-76) in the human ferrochelatase. Bacterial and human ferrochelatase are highly conserved at the level of tertiary structure although there is less than 10 % conservation at the level of amino acid sequence. Furthermore, their core regions are also similar. In *Bacillus subtilis* ferrochelatase, the position of the residue Met-76 is replaced by the Tyr-13. The oxygen atom of Tyr-13 may coordinate with Fe^{2+} and could probably play a key role on transferring Fe^{2+} to the center of protoporphyrin IX. Therefore, there is a possibility for Fe^{2+}

insertion from the side of Tyr-13. In this work, we use combined quantum mechanics and molecular mechanics (QM/MM) calculations to simulate this process and try to illustrate possibility of this path.

Methods

QM/MM approach

The COMQUM software [16, 17] was used for the QM/MM optimizations and single point energy calculations with large basis set. To build QM/MM model, the whole system (include the protein and solvent) is divided into three regions (Fig. 1a): system 1 consists of the porphyrin ring, Fe^{2+}, Tyr-13, His-88, His-183, Glu-264 and six crystal water molecules (see Fig. 1b) and quantum mechanics (QM) method is used for its calculation. All the atoms except for constrained atoms and junction atoms are allowed to move freely during optimization; System 2 contains all residues with any atom within 6 Å of any atom in system 1, and is optimized by molecular mechanics (MM). The remaining portion of the protein and the water molecules surrounding the enzyme are included in system 3, which is kept fixed at the crystal coordinates. MM method is also employed in this part for energy calculation. The Turbomole software [18, 19] is used for the QM part, and Amber 7 [20, 21] (with the Amber 1999 force field [22]) is used for the MM part. This approach is similar to the one used in the Oniom method [23]. In such a hybrid method, covalent bonds between systems 1 and 2 are treated by the link-atom approach [16]: the QM system is truncated by hydrogen atoms, the positions of which reference on the positions of corresponding carbon atoms in the protein. The total QM/MM energy is calculated based on the following equation.

$$E_{QM/MM} = E_{QM} + E_{MM123} - E_{MM1}$$

Here, E_{QM} is the QM energy of the quantum system truncated by hydrogen atoms, including the interaction between system 1 and the surroundings, modeled by point charges. E_{MM1} is the MM energy of the quantum system, still truncated by hydrogen atoms, but without any electrostatic interactions. E_{MM123} is the classical energy of all the atoms in the system with carbon atoms at the junctions and with the charges of the QM region zeroed, to avoid double counting of the electrostatic interactions.

The geometry optimizations were carried out in three steps. First, only the quantum system was optimized and systems 2 and 3 were fixed. Second, both systems 1 and 2 were allowed to relax. In this optimization, the charges on the quantum atoms in the MM minimization were updated in each iteration of the optimization. This calculation was performed with the looser convergence criteria of 10^{-4} a.u. for the change in energy and 10^{-2} a.u. for the maximum norm of Cartesian gradient. Finally, system 2 was fixed again and the geometry optimization was continued with default convergence criteria (10^{-6} and 10^{-3} a.u.). If not otherwise stated, our discussion is based on the final step calculations, because these structures are expected to be more realistic.

The protein

The crystal structure of *Bacillus subtilis* ferrochelatase in complex with the inhibitor N-methylmesoporphyrin (MMP), PDB code 1C1H (1.9 Å resolution) is used for building QM/MM model [7]. This structure was selected because it is the structure of *Bacillus subtilis* ferrochelatase with a bound porphyrin. Although the crystal structure of human ferrochelatase with porphyrin shows a different binding mode, the structure we used here is in a "productive" state which indicates that the site of MMP reflects the real binding position of protoporphyrin IX. It is probably the factors and the helix length that affect the position of protoporphyrin IX which make the human and *Bacillus subtilis* exibit different binding modes [24].

The QM/MM model was built by removing the methyl group of MMP and converting the two ethyl side chains back to vinyl groups (giving protoporphyrin IX), and by

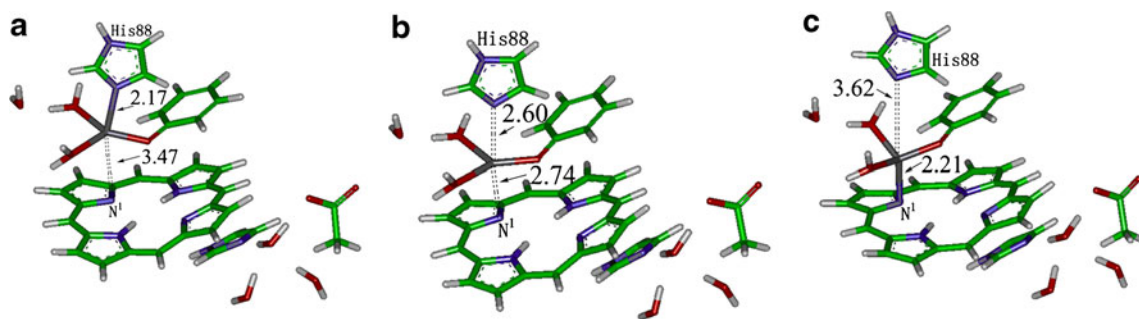Fig. 1 **a** Three regions for QM/MM calculation; **b** The initial structure of QM system
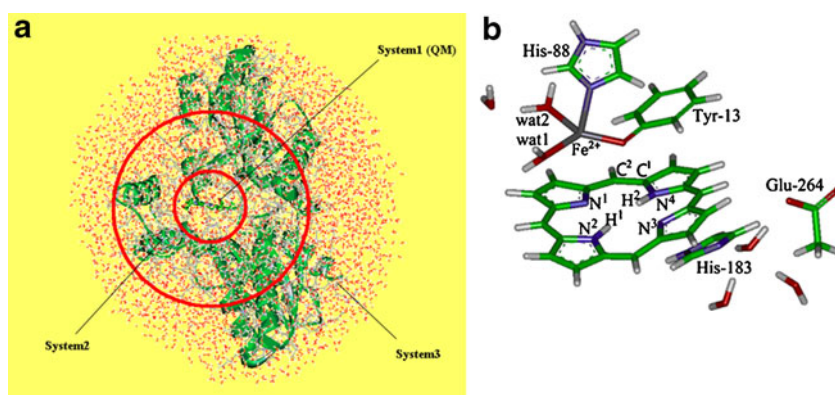
Fig. 2 Dissociation of the Fe-N$_{His-88}$ bond and formation of the Fe-N^1 bond, optimized at the QM/MM level. **a** Initial model without any constraints. **b** The structure with the highest energy. **c** The structure with Fe-N^1 bond formed, without any constraints

adding a Fe^{2+} ion coordinated with Tyr-13, His-88 and two water molecules. All residues were assumed to be in their most stable protonation state at neutral pH. Thus, all Arg and Lys residues were considered in their protonated state, whereas all Asp and Glu residues were considered in their deprotonated states. After a detailed study of the surroundings and possible hydrogen-bond networks around the His residues, it was decided that His-88, 116, 183, and 262 were protonated on the N$^{\delta 1}$ atom, His-28 was protonated on the N$^{\varepsilon 2}$ atom, and the remaining His residues were doubly protonated. Hydrogen atoms were added to the protein by

the Amber software and the protein was solvated in a sphere of water molecules with a radius of 37 Å. 18 Na$^+$ ions were added to neutralize the charges of the system. All hydrogen atoms, Na$^+$ ions, and the solvent water molecules were equilibrated by a simulated annealing molecular dynamics calculation (raising the temperature from 0 to 300 K in 10 ps, keep in 300 K for 80 ps, and re-cool from 370 K to 0 K in 160 ps) and followed by 10,000 steps of conjugate gradient energy minimization. The total simulated system had 16,991 atoms with 94 atoms in the QM region. The QM system consisted of the Fe^{2+} ion, the porphyrin ring without

Fig. 3 Three pathways: Formation of the H^1-N^3 and H^2-N^3 bonds and dissociation of Fe^{2+}-O$_{wat1}$ bond respectively, optimized with QM/MM method. **a** The first structure. **b** Formation of the H^1-N^3 bond. **c** Formation of the H^2-N^3 bond. **d** Dissociation of Fe^{2+}-O$_{wat1}$ bond

H^1–N^3
58.61KJ/mol

H^2–N^3
31.03KJ/mol

−wat1
35.13KJ/mol
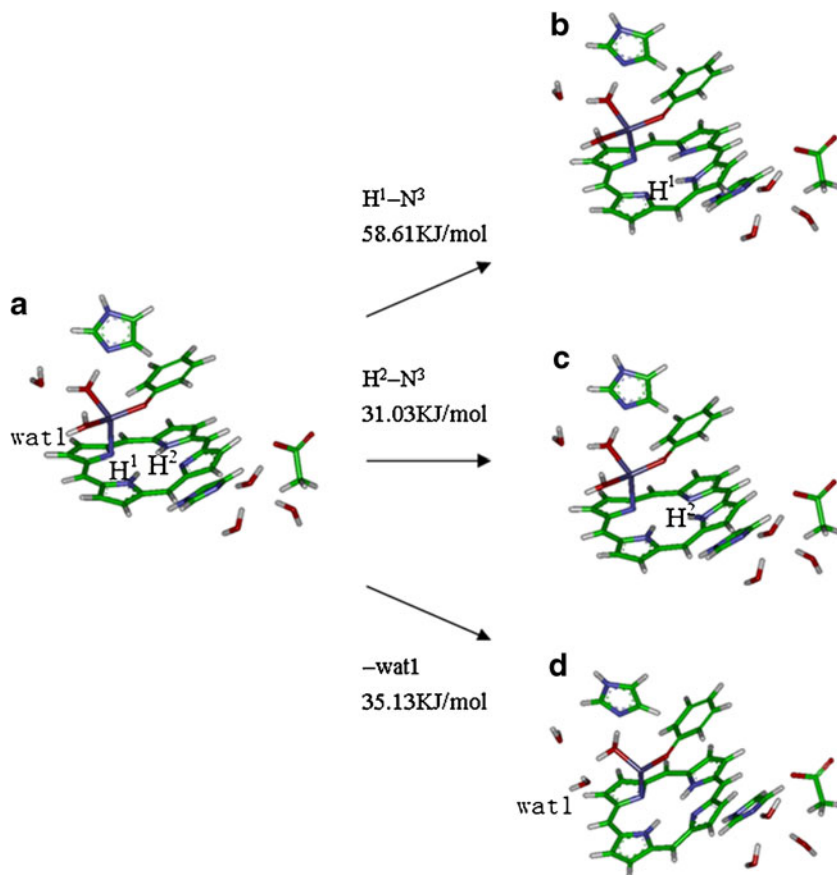
any side chains, Tyr-13 modeled as phenolate, the imidazole side chain of the His-88 and His-183, Glu-264 modeled as acetate, and six crystal water molecules (Fig. 1b).

Quantum-chemical calculations

The geometry optimization of the QM region was carried out with the Turbomole software [18, 19]. The 6-31G* basis set was employed for C, N, O, H atoms, the DZpdf basis set for Fe [25]. Moreover, we applied the resolution of identity (RI) approximation [26, 27] to speed up the calculations by a factor of ~10. After the QM/MM geometry optimizations, we performed a single-point calculation at the B3LYP/6-311+G(2d,2p) (Fe still described by the

DZpdf basis set) level, which was expected to give more reliable QM energies [28–31]. Density functional methods have been shown to give excellent geometries for transition-metal complexes (including heme models with various axial ligands), with errors in the bond distances of 0–7 pm [32–34]. A quintet spin state was employed for all models, using unrestricted formalism.

Results and discussion

There are two possible initial sites for Fe^{2+} inserting into the porphyrin. Site 1: coordinates with His-183 and Glu-264. Site 2: coordinates with Tyr-13 and His-88 on the opposite site of His-183. We have reported the simulation of the

Fig. 4 The various structures along the five possible pathways. **a** Pathway I and II. **b** Pathway III, IV and V
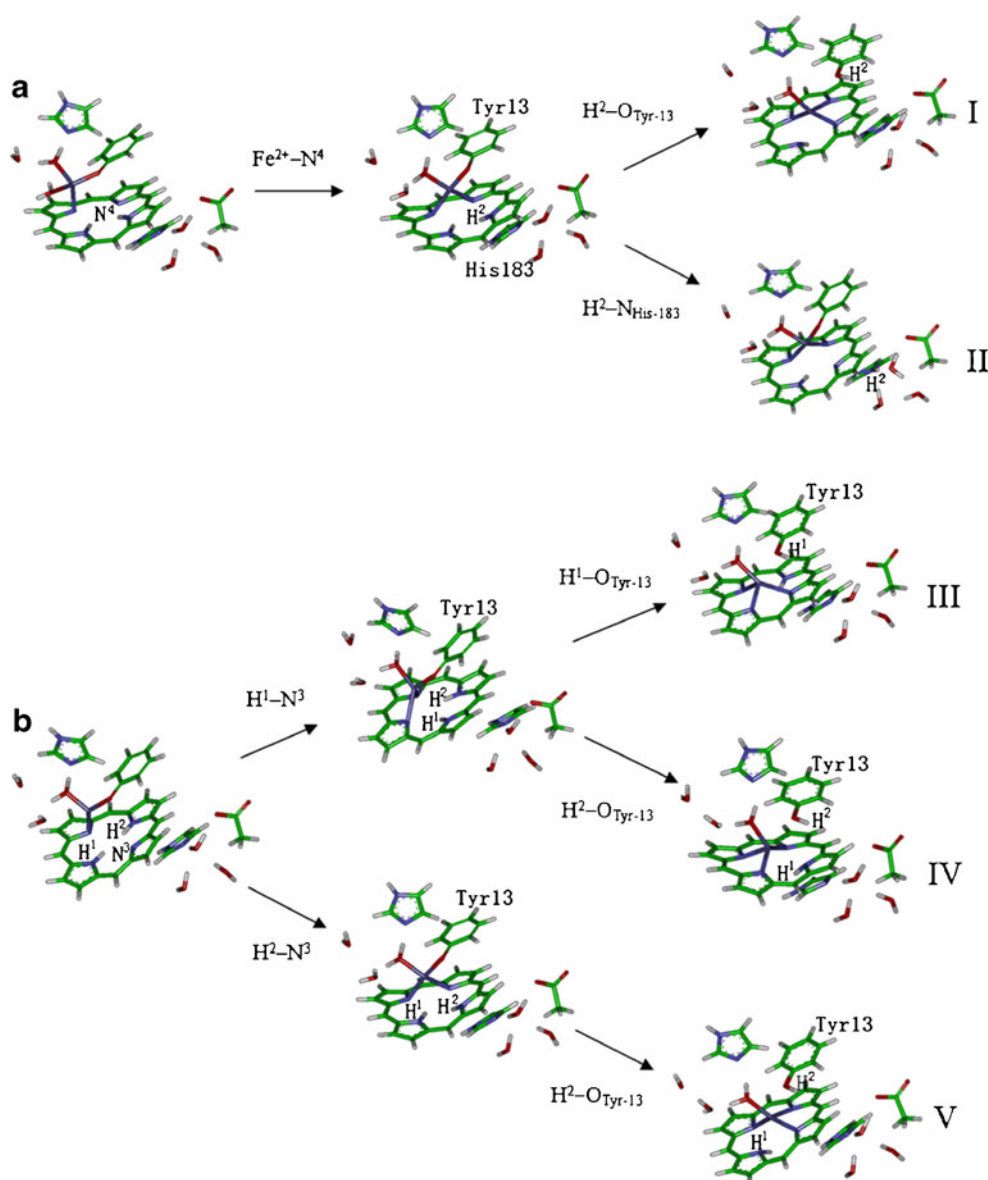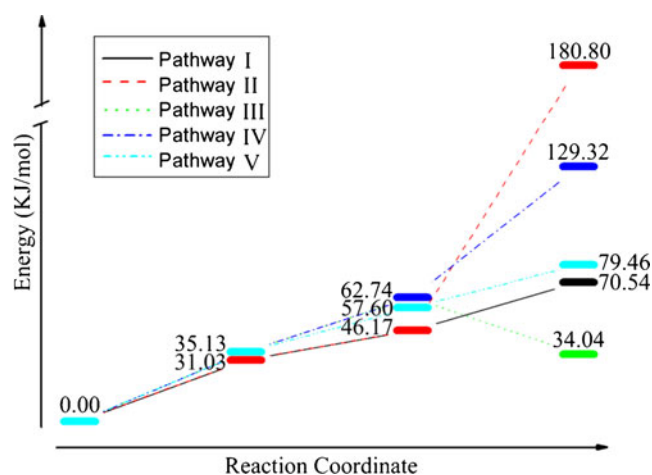
insertion process from site 1 [14]. In this paper, we will simulate the insertion process from site 2 by QM/MM method. The ferrous ion has a preference to form six coordinated complexes. So we built the initial model with six ligands coordinating with Fe^{2+}. However, after the QM/MM optimization, only four ligands could coordinate with Fe^{2+} and two water molecules go away. The reason for this is probably the small space between Fe^{2+} and the porphyrin ring. Therefore, we built our initial model with Fe^{2+} bounded with Tyr-13 and His-88 and two water molecules, shown in Fig. 2a. His-183 and Glu-264 were included in QM system for extracting the proton from the porphyrin ring. Four additional water molecules (which do not bind directly to Fe^{2+}) were also included, because they form hydrogen bonds with the residues and the Fe-bound water molecules in the QM system.

Formation of the first Fe-N bond

Based on the first model (Fig. 2a), we moved Fe^{2+} close to N^1 atom of the porphyrin ring by constraining the Fe-N^1 distance step by step to simulate the formation process of the Fe-N^1 bond. After obtaining the potential energy surface curve along the reaction coordinate, we continue our constraint back and forth on the points around the highest point
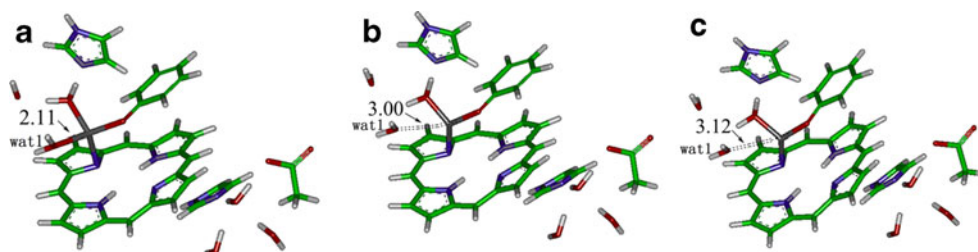
to determine the point with the highest energy. With the decrease of the distance of Fe and N^1, Fe-N_{His-88} bond length was elongated. In the highest energy state (Fig. 2b) along the reaction pathway, the distances of Fe-N_{His-88} and Fe-N^1 are 2.60 and 2.74 Å, respectively. At last, the Fe-N^1 bond formed with a bond length of 2.21 Å and the Fe-N_{His-88} bond was dissociated with a large Fe-N_{His-88} distance (3.62 Å) (Fig. 2c). The atom N^1 stays in the plane of porphyrin ring in Fig. 2a and tilts up a very small angle (<5°) in Fig. 2b and c which is smaller than the one (~10°) while Fe^{2+} enters into the porphyrin from the opposite side. The energy barrier of this process is 11.57 kJ/mol at the BP86/6-31G* level (the same level used in the following energies if not specified), and the energy increases to 24.26 kJ/mol at the B3LYP/6-311+G(2d,2p) level. This barrier is much less than that while Fe^{2+} approaches the protoporphyrin IX from the opposite side. It is easy to see that the small tilt angle of the N^1 atom does not increase the barrier. Instead, the barrier energy decreases 33kJ/mol more than the one in the opposite path. The decrease of the barrier may be due to the easier cleavage of Fe-N than that of Fe-O. Comparing with the previous transition state structure, the two structures both have trigonal bipyramidal configuration. However, Fig. 2 shows that both the breaking bond Fe-N_{His88} and forming bond Fe-N^1 are in the axial direction, and in the previous model, the breaking bond Fe-O is in the equator direction while only Fe-N^1 is in the axial direction. So, the weaker axial bond probably plays a key role on lowering the barrier energy. The bond lengths and relative energies are shown in Table S1.

Analyzing the possible ways for forming the second Fe-N bond and deprotonation

The next step in the reaction mechanism would be the formation of the second Fe-N bond. We have tried to simulate the formation of the second Fe-N bond with N^2, N^3 and N^4, respectively. However, the energies always go up and there are no stable local minimum structures during these processes. So, direct formation of the second Fe-N bond is impossible. Transferring proton or removing one water ligand from Fe^{2+} might lower the energy barrier of formation of the second Fe-N bond, We have tried to re-
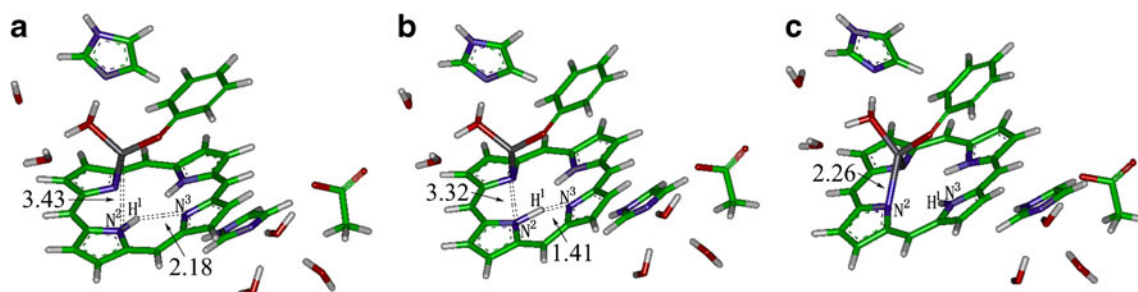

Fig. 6 Dissociation of the Fe-O_{wat1} bond, optimized at the QM/MM level. **a** Initial model without any constraints. **b** The structure with the highest energy. **c** The structure with Fe-O_{wat1} bond broken, without any constraints

Fig. 7 Formation of the H^1-N^3 and Fe^{2+}-N^2 bonds, optimized at the QM/MM level. **a** Initial model without any constraints. **b** The structure with the highest energy. **c** The structure with H^1-N^3 and Fe^{2+}-N^2 bonds formed, without any constraints

move one proton by $N_{His-183}$ and O_{Tyr-13} respectively before forming the second Fe-N bond. However directly transferring proton to $N_{His-183}$ leads to a rather high barrier (>200 kJ/mol) and to O_{Tyr-13} no stable local minimum structure. So, there are three possible ways left before the formation of the second Fe-N bond. First, H^1 transferred to N^3 (Fig. 3b). This led to a small high energy barrier (58.61 kJ/mol). Second, H^2 transferred to N^3 (Fig. 3c). The energy barrier was 31.03 kJ/mol. Third, we removed one water by constraining the Fe-O_{wat1} distance from 2.11 to 3.12 Å (Table S1), which led to the dissociation of the Fe-O_{wat1} bond with an energy barrier of 35.13 kJ/mol (Fig. 3d).

Comparing the three possible ways, the first way can be rejected because of the high energy barrier. So we continued the simulation based on models c and d (Fig. 3). There are five possible ways to form the second Fe-N bond (Fig. 4).

Pathway I: We constrained the distance of Fe^{2+} and N^4 to form Fe-N bond while the Fe^{2+}-O_{wat1} bond was broken. The energy barrier was 46.17 kJ/mol. For the next step, Fe^{2+} maybe form the third and fourth Fe-N bond. However, continued Fe-N bond forming steps could not happen when the two protons stay on the porphyrin ring. So, the next step should be the proton removing. There are two candidate atoms (O_{Tyr-13} and $N_{His-183}$) to accept the proton. In this pathway, H^2 was transferred from N^3 to O_{Tyr-13}, the Fe^{2+}-O_{Tyr-13} bond was

broken and the Fe^{2+}-N^3 bond formed. The energy barrier was 70.54 kJ/mol (Fig. 4a).

Pathway II: The same as pathway I but H^2 transferred from N^3 to $N_{His-183}$. The energy barrier was rather high (180.80 kJ/mol) (Fig. 4a) due to the long distance between the two atoms. In the next pathways, we would not consider removing the first proton from prophyrin by residue His-183, because it had too high an energy barrier.

Pathway III: Transferring H^1 to N^3 and the Fe^{2+}-N^2 bond concomitantly formed with energy barrier 62.74 kJ/mol. Next, transferring H^1 from N^3 to O_{Tyr-13}, the Fe^{2+}-O_{Tyr-13} bond was broken and the bond of Fe^{2+}-N^3 formed at the same time. The energy barrier was 34.04 kJ/mol (Fig. 4b).

Pathway IV: The same as pathway III but H^2 transferred to O_{Tyr-13} and the bond of Fe^{2+}-N^4 formed with higher energy barrier 129.32 kJ/mol (Fig. 4b).

Pathway V: Transferring H^2 to N^3, the Fe^{2+}-N^4 bond concomitantly formed. The energy barrier is 57.60 kJ/mol. Next, transferring H^2 from N^3 to $O_{Tyr-13,}$ the Fe^{2+}-O_{Tyr-13} bond was broken and the Fe^{2+}-N^3 bond formed at the same time. The energy barrier was 79.46 kJ/mol (Fig. 4b).

The relative energies of the various structures along the five possible pathways are shown in Fig. 5. Pathway II
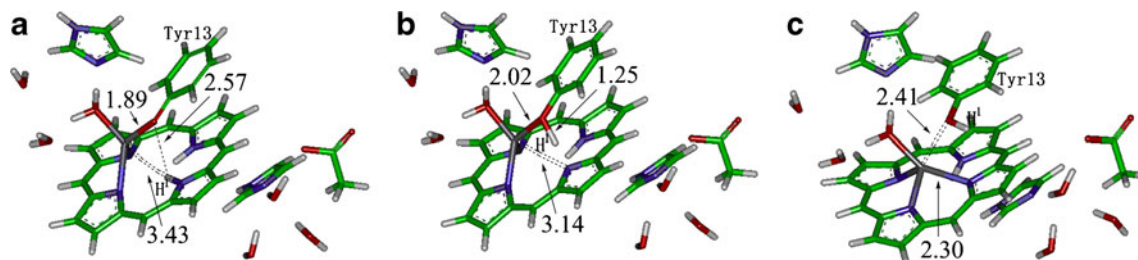

Fig. 8 Formation of the H^1-O_{Tyr-13} and Fe^{2+}-N^3 bonds; Dissociation of the bond of Fe^{2+}-O_{Tyr-13}, optimized at the QM/MM level. **a** Initial model without any constraints. **b** The structure with the highest energy. **c** The structure with H^1-N^3 and Fe^{2+}-N^3 bonds formation, without any constraints
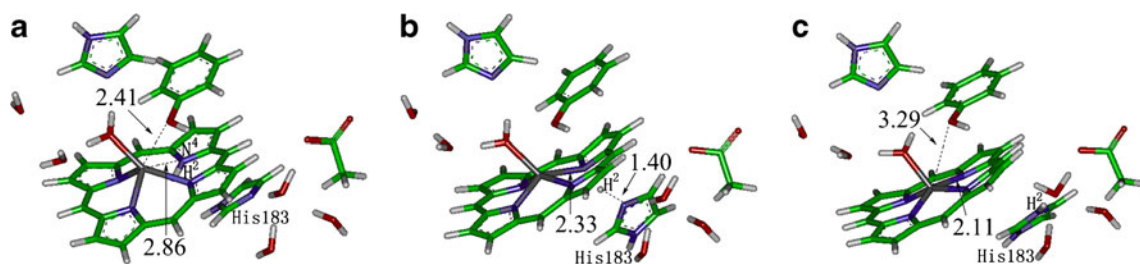
Fig. 9 Deprotonation H^2 and formation of the bond of Fe^{2+}-N^4, optimized at the QM/MM level. **a** Initial model without any constraints. **b** The structure with the highest energy. **c** The structure with H^2-$N_{His-183}$ and Fe^{2+}-N^4 bonds formation, without any constraints

shows the highest barriers among all the pathways which indicates that quite a long distance from the proton makes the $N_{His-183}$ incompetent as a proton acceptor. The relatively high barrier in pathway IV could be ascribed to the strain energy induced by their relative site which makes the forming bond (H- O_{Tyr-13}) bend almost vertical to the normal direction. Although the barrier energies in pathway I and pathway V are moderate, the structures show that the second proton could only be removed by $N_{His-183}$ and not by O_{Tyr-13} because the Fe atom stays between them, which would increase the barrier to quite a high value. Thus, the pathway III is a top priority pathway, which will be particularly interpreted as the following.

Formation of the second Fe-N bond

After the first Fe-N bond formation (Fig. 6a), we constrained the Fe-O_{wat1} distance from 2.11 to 3.12 Å (Table S1), which led to the dissociation of the Fe-O_{wat1} bond with an energy barrier of 35.13 kJ/mol (43.12 kJ/mol at the B3LYP/6-311+G (2d,2p) level). Figure 6b shows the structure with the highest energy along the reaction pathway. In this structure, the distance of Fe-O_{wat1} is 3.00 Å. Figure 6c shows the structure of the intermediate with Fe-O_{wat1} bond broken (3.12 Å). It was optimized without any constraints.

Then, we constrained the H^1-N^3 distance from 2.18 to 1.02 Å (Fig. 7). During this process, the Fe^{2+}-N^2 bond con-
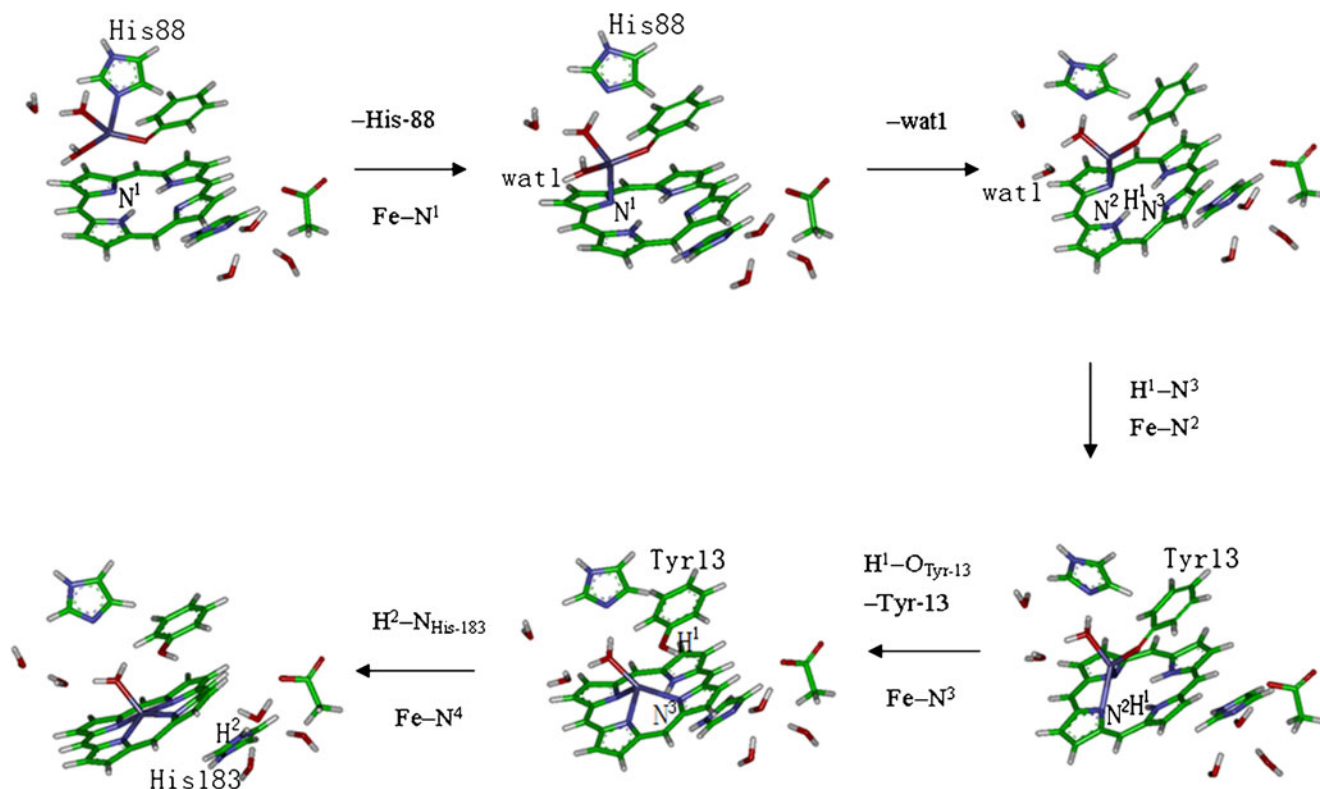
Scheme 1 The overall metallation process

comitantly formed (the bond length is 2.26 Å, Fig. 7c). Figure 7b shows the structure with the highest energy along the reaction pathway (the distances of Fe^{2+}-N^2 and H^1-N^3 are 3.32 and 1.41 Å, respectively). The energy barrier is 62.74 kJ/mol (72.81 kJ/mol at the B3LYP/6-311+G(2d,2p) level).

Formation of the third and fourth Fe-N bonds

Next, we tried to remove the protons of the porphyrin ring. As shown in Fig. 8a, we simulated H^1 transferred from N^3 to $O_{Tyr\text{-}13}$. During this process, the Fe^{2+}-$O_{Tyr\text{-}13}$ bond was broken and the Fe^{2+}-N^3 bond formed. Figure 8b shows the structure with the highest energy along the reaction pathway. The distances of Fe^{2+}-N^3, Fe^{2+}-$O_{Tyr\text{-}13}$ and H^1-$O_{Tyr\text{-}13}$ are 3.14, 2.02 and 1.25 Å, respectively. Figure 8c shows the structure of the intermediate with Fe-$O_{Tyr\text{-}13}$ bond broken (2.41 Å) and Fe^{2+}-N^3 bond formed (2.30 Å). It is optimized without any constraints. The energy barrier is 34.04 kJ/mol (31.74 kJ/mol at the B3LYP/6-311+G(2d,2p) level). The $H^2N^4C^1C^2$ torsion angle changed from $-9.00°$(Fig. 8a) to $21.25°$(Fig. 8c, the atom names are defined in Fig. 1). This means that the H^2 atom in the structure in Fig. 8c tilts down much more than that in Fig. 8a, which makes H^2 atom closer to $N_{His\text{-}183}$ and easier to be extracted by it. In the meantime, the distance between the H^2 atom and the $O_{Tyr\text{-}13}$ is enlarged, which makes it hard for $O_{Tyr\text{-}13}$ to accept the proton. Furthermore, the relative site of the two atoms (H^2 and $O_{Tyr\text{-}13}$) will largely increase the barrier (see above discussion for pathway IV). So the barrier energy for $O_{Tyr\text{-}13}$ to extract the proton should be larger than that of pathway IV. So, for the next step, we will only focus on the $N_{His\text{-}183}$ as proton acceptor because of the possible low barrier induced by the proton tilting down.

Based on the last structure from the last step (Fig. 9a), we constrained the H^2-$N_{His\text{-}183}$ distance from 4.15 to 1.10 Å (Table S1). When the H^2-$N_{His\text{-}183}$ distance was 1.40 Å, the fourth Fe-N bond formed (Fig. 9b). Figure 9c shows the structure of the intermediate with Fe^{2+}-N^4 bond formed (2.11 Å). The lower energy barrier 119.23 kJ/mol (138.00 kJ/mol at the B3LYP/6-311+G(2d,2p) level) which is 60 kJ/mol lower than that of pathway II indicates that change of the H^2 position makes the H^2-$N_{His\text{-}183}$ bond easier to form. At last, the Fe^{2+} falls into the center of the protoporphyrin IX with one water molecule coordinated. The four Fe-N bond and Fe-O_{wat2} lengths are 2.06, 2.04, 2.18, 2.11 and 2.09 Å, respectively, which indicates the Fe atom sitting in the porphyrin plane other than a sitting atop structure.

From the above discussion, we could see that the proton should be removed stepwise from two sides of the porphyrin by different residues rather than by one residue (Tyr13) as in the previous study. Especially for the second proton transferring, it is obviously impossible for $O_{Tyr\text{-}13}$ to accept the
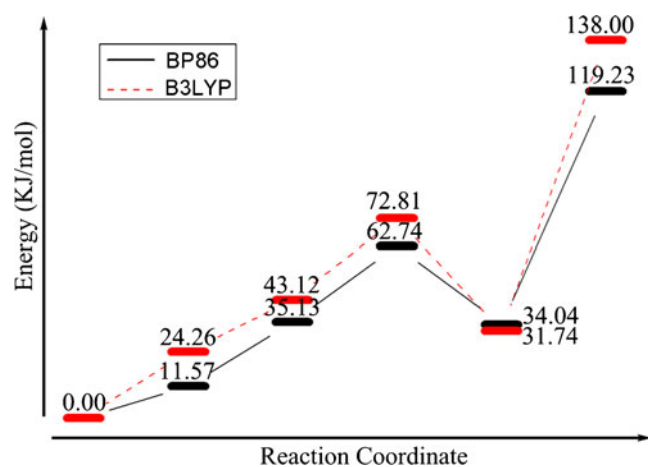

Fig. 10 The relative energies of the various structures along the overall metallation process. (The structures are shown in Fig. 9)

proton because of H^2 tilting down and its position makes the barrier quite high. Although barrier could be decreased by $N_{His\text{-}183}$ extracting H^2, the absolute value of the barrier (138 kJ/mol) is much higher than the barrier (57.46 kJ/mol) in our previous study with Fe^{2+} coming from the opposite side. The reason maybe due to two aspects: one is the distance between H^2 and $N_{His\text{-}183}$ is very long (~4 Å). The other one, probably the most important one, is that $N_{His\text{-}183}$ stay under porphyrin. This sort of alignment makes the forming bond and the breaking bond not sit in a line and N-H^2 bends to a large degree before forming the transition state structure (Fig. 9b) which should contribute much to the barrier increase. Therefore, the high barrier makes the pathway from the side of Tyr-13 unfeasible.

Conclusions

In the present study, we simulated the process of ferrous ion inserting into the protoporphyrin IX from the side of residue Tyr-13 in *Bacillus subtilis* ferrochelatase. The whole process could be described as Scheme 1: the bond of Fe^{2+}-$N_{His\text{-}88}$ is broken and the first Fe-N bond forms; the water molecule dissociates from Fe^{2+}; the first proton H^1 transfers to N^3 and the second Fe-N bond forms; H^1 transfers from N^3 to $O_{Tyr\text{-}13}$, the residue Tyr-13 dissociates and the third Fe-N bond forms; the second proton H^2 is removed by the residue His-183, the fourth Fe-N bond forms. The residues Tyr-13 and His-183 extract the two protons from the porphyrin ring respectively. The relative energies of the various structures along the metallation pathways are shown in Fig. 10. The second deprotonation of the porphyrin ring is the rate-determining step with a barrier of 138.00 kJ/mol which is larger than the one in our previous report where the Fe^{2+} ion inserts into the porphyrin from the opposite side of the

residue Tyr-13 (Fe^{2+} coordinated with His-183 and Glu-264) and the rate-determining step is the formation of the first Fe-N bond with the energy barrier of 57.46 kJ/mol.

References

1. Dailey HA, Dailey TA (2003) Ferrochelatase. In: Kadish KM, Smith KM, Guilard R (eds) The porphyrin handbook. Academic, New York, pp 93–121
2. Chen FP, Risheg H, Liu YY, Bloomer J (2002) Cell Mol Biol 48:83–89
3. Sassa S, Zalar GL, Poh-Fitzpatrick MB, Anderson KE, Kappas A (1982) J Clin Invest 69:809–815
4. Cox TM (1997) J Inherit Metab Dis 20:258–269
5. Daily HA, Fleming JE (1983) J Biol Chem 258:11453–11459
6. Baum SJ, Plane RA (1966) J Am Chem Soc 88:910–913
7. Lecerof D, Fodje M, Hansson A, Hansson M, Al-Karadaghi S (2000) J Mol Biol 297:221–232
8. Dailey HA, Dailey TA, Wu CK, Medlock AE, Wang KF, Rose JP, Wang BC (2000) Cell Mol Life Sci 57:1909–1926
9. Wu CK, Dailey HA, Rose JP, Burden A, Sellers VM, Wang BC (2001) Nat Struct Biol 8:156–160
10. Karlberg T, Lecerof D, Gora M, Silvegren G, Labbe-Bois R, Hansson M, Al-Karadaghi S (2002) Biochemistry 41:13499–13506
11. Medlock A, Swartz L, Dailey TA, Dailey HA, Lanzilotta WN (2007) Proc Natl Acad Sci U S A 104:1789–1793
12. Hansson MD, Karlberg T, Rahardja MA, Al-Karadaghi S, Hansson M (2007) Biochemistry 46:87–94
13. Ferreira GC, Franco R, Mangravita A, George GN (2002) Biochemistry 41:4809–4818
14. Wang YX, Shen Y, Ryde U (2009) J Inorg Biochem 103:1680–1686
15. Sellers VM, Wu CK, Dailey TA, Dailey HA (2001) Biochemistry 40:9821–9827
16. Ryde U (1996) J Comput Aided Mol Des 10:153–164
17. Ryde U, Olsson MHM (2001) Int J Quantum Chem 81:335–347
18. Ahlrichs R, Bär M, Häser M, Horn H, Kölmel C (1989) Chem Phys Lett 162:165–169
19. Hertwing RH, Koch W (1997) Chem Phys Lett 268:345–351
20. Weiner SJ, Kollman PA, Nguyen DT, Case DA (1986) J Comput Chem 7:230–252
21. Weiner SJ, Kollman PA, Case DA, Singh UC, Ghio C, Alagona G, Profeta S, Weiner P (1984) J Am Chem Soc 106:765–784
22. Cornell WD, Cieplak P, Bayly CI, Gould IR, Merz KM, Ferguson DM, Spellmeyer DC, Fox T, Caldwell JW, Kollman PA (1995) J Am Chem Soc 117:5179–5197
23. Svensson M, Humbel S, Froese RDJ, Matsubara T, Sieber S, Morokuma K (1996) J Phys Chem 100:19357–19363
24. Karlberg T, Hansson MD, Yengo RK, Johansson R, Thorvaldsen OH, Ferreira GC, Hansson M, Al-Karadaghi S (2008) J Mol Biol 378:1074–1083
25. Sigfridsson E, Ryde U (2003) J Biol Inorg Chem 8:273–282
26. Eichkorn K, Treutler O, Öhm H, Häser M, Ahlrichs R (1995) Chem Phys Lett 240:283–290
27. Eichkorn K, Weigend F, Treutler O, Ahlrichs R (1997) Theor Chem Acc 97:119–124
28. Claeyssens F, Harvey JN, Manby FR, Mata RA, Mulholland AJ, Ranaghan KE, Schutz M, Thiel S, Thiel W, Werner HJ (2006) Angew Chem Int Ed 45:6856–6859
29. Siegbahn PEM, Blomberg MRA (1999) Annu Rev Phys Chem 50:221–249
30. Himo F (2006) Theor Chem Acc 116:232–240
31. Bauschlicher CW (1995) Chem Phys Lett 246:40–44
32. Sigfridsson E, Olsson MHM, Ryde U (2001) J Phys Chem B 105:5546–5552
33. Olsson MHM, Ryde U (2001) J Am Chem Soc 123:7866–7876
34. Ryde U, Nilsson K (2003) J Am Chem Soc 125:14232–14233